

Optimal Exploration Target Zones

Pravesh Debba¹, Emmanuel M.J. Carranza², Alfred Stein², Freek D. van der Meer²

¹CSIR, Logistics and Quantitative Methods, CSIR Built Environment, P.O. Box 395, 0001, South Africa, pdebba@csir.co.za / pdebba@gmail.com

²International Institute for Geo-Information Science and Earth Observation (ITC), Hengelosestraat 99, P.O. Box 6, 7500AA Enschede, The Netherlands, carranza@itc.nl, stein@itc.nl, vdmeer@itc.nl

Abstract

This research describes a quantitative methodology for deriving optimal exploration target zones based on a probabilistic mineral prospectivity map. A subset of known occurrences of mineral deposits of the type sought were considered discovered and then used as training data, and a map of distances to faults/fractures and three band ratio images of hyperspectral data were used as layers of spatial evidence in weights-of-evidence (WofE) modeling. This resulted in a mineral prospectivity map, which is based on a Bayesian probability framework to update the prior probability of mineral deposit occurrences of the type sought in every unit cell or pixel in a study area. The derived posterior probability map of mineral deposit occurrence was then input to an objective function in simulated annealing in order to derive a set of optimal exploration focal points. An optimal exploration focal point is a pixel or location, at and around which there is high posterior probability of mineral deposit occurrences. Buffering of each optimal exploration focal point, results in optimal exploration target zones, many of which coincide spatially with at least one of the occurrences of the mineral deposit in the subset of cross-validation (i.e., presumed undiscovered) mineral deposits. The results of the study show usefulness of the proposed methodology for objective delineation of optimal exploration target zones and are demonstrated in the Rodalquilar mineral district in Spain.

1. Introduction

Occurrences of mineral deposits, which could be in the form of mines, prospects or even showings, are considered samples of a mineralized landscape. Occurrences of mineral deposits of the type sought are used for training in data-driven predictive mapping of mineral prospectivity. Basically, mineral prospectivity mapping is a tool for delineating of targets, whereabouts probability for occurrence of mineral deposit-type of interest is high, which might warrant more detailed survey in a further stage of mineral exploration. In regional- to district-scale mineral prospectivity mapping the objective is to delineate exploration target zones (polygons), whereas in local- to deposit-scale the objective is to define exploration target locations (points). A logical question regarding usefulness of a regional- to district-scale mineral prospectivity map is: “Which areas are optimal exploration target zones for further surveying of undiscovered occurrences of the

mineral deposit-type sought?”

The objective of this paper is to demonstrate a methodology to provide a plausible answer to the question in a district-scale case study. Because mineral deposit occurrences can be considered samples of a mineralized landscape, a configuration of exploration focal points can also be considered as a sampling scheme. We tested our proposed methodology, to derive optimal exploration target zones from a district-scale mineral prospectivity map, within the Rodalquilar mineral district in Spain.

2. Study Area and Data Used

2.1 Geology and Mineralization of the Rodalquilar Mineral District

The Rodalquilar mineral district is located in the Sierra del Cabo de Gata volcanic field, in the south-eastern part of Spain (Fig. 1), consisting of pyroxene andesites to rhyolites of the late Tertiary age. Extensive hydrothermal alteration of the volcanic rocks resulted in formation of high to low temperature minerals as: silica→alunite→kaolinite→illite→chlorite. Occurrences of high- or low-sulphidation epithermal precious- and base-metal deposits are in veins or in hydrothermal breccias (i.e. fracture controlled) associated with hydrothermally altered rocks (Arribas et al., 1995). High-sulphidation precious-metal deposits are associated with advanced argillic (alunite±kaolinite) and intermediate argillic (kaolinite±illite) zones, whereas low-sulphidation precious- and base-metal deposits are associated with argillic to pyrophyllitic (illite±chlorite) zones (Arribas et al., 1995). The epithermal minerals are localized along faults and fractures that cut through the volcanic host rocks. Based on these generalized geological characteristics of the discovered occurrences of epithermal mineral deposits in the district, we apply two recognition criteria in mapping prospectivity for epithermal mineral deposits, (1) hydrothermal alteration evidence and (2) structural evidence.

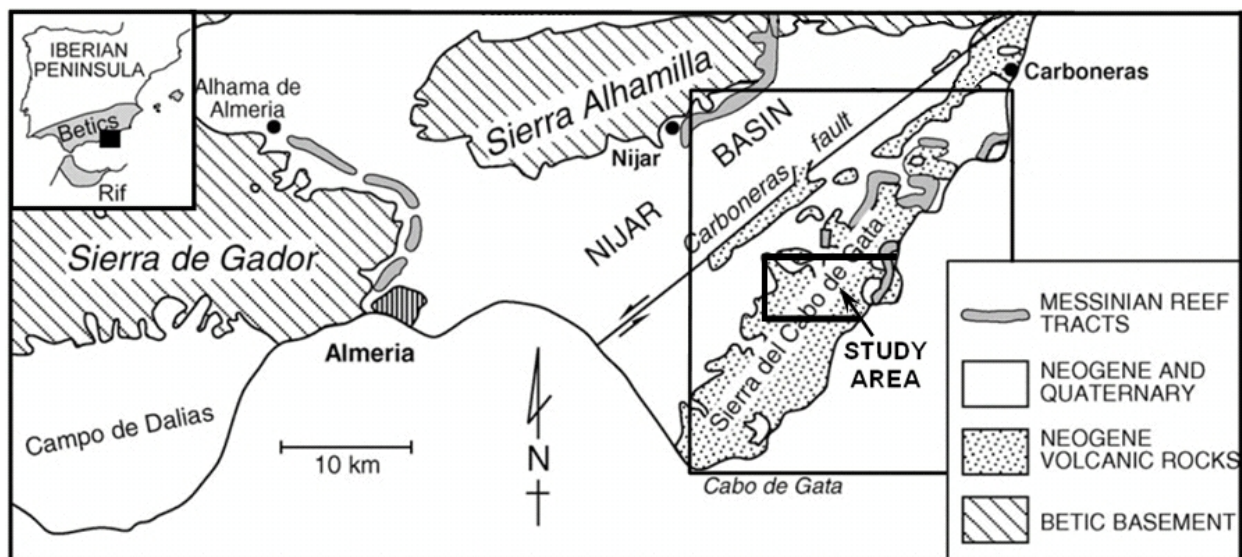


Figure 1: A generalized geological map of the Rodalquilar area mineral district.

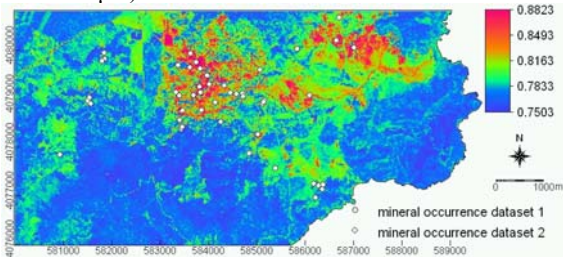
2.2 Data for Hydrothermal Alteration Evidence

We used a sub-scene, consisting of 2640×1300 pixels, of airborne imaging spectrometer data acquired by the Hyperspectral Mapper (HyMAP) in July 2003. HyMap is a 126-band sensor that records the reflected solar radiation within the $0.4\text{--}2.5\ \mu\text{m}$ wavelength region of the electromagnetic spectrum. Data acquired by the shortwave-infrared (SWIR) 2 detector, within the $1.95\text{--}2.48\ \mu\text{m}$ spectral range covers the most prominent spectral absorption features of hydroxyl-bearing minerals, sulfates and carbonates, which are common to many hydrothermal alteration assemblages (Kruse, 2002). SWIR 2 data are useful for mapping hydrothermal alteration assemblages as well as for regolith characterization (Cudahy et al., 2000; Kruse, 2002).

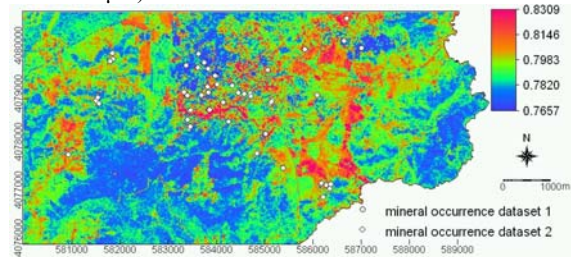
In order to delineate predominant minerals in hydrothermal alteration zones associated with the epithermal deposits, hyperspectral band ratio images (Lillesand et al., 1994) were created. Band ratioing is a way to enhance the presence of a material of interest from spectral images by dividing data in a spectral band with data in another spectral band. We used an arctan transformation on the band ratios (Lillesand et al., 1994), which considers the gradient of spectral data between two bands. Figure 2 display the band ratio images used as evidence layers in the weights-of-evidence (WofE) modeling.

Pixels in the image of band ratio 1 ($2.100/2.171\ \mu\text{m}$) are brighter (i.e. higher ratios) for alunite, kaolinite and pyrophyllite but slightly darker (i.e. lower ratios) for illite (Fig. 2A). The first three minerals are predominant in advanced argillic zones. For band ratio 2 ($2.171/2.205\ \mu\text{m}$) pixels are brighter for illite and kaolinite but are darker for alunite and pyrophyllite (Fig. 2B). The brighter pixels in this image thus enhance predominant minerals associated with intermediate argillic zones. Pixels in the image of band ratio 3 ($2.357/2.258\ \mu\text{m}$) are darker for minerals predominant in advanced argillic zones but brighter for minerals predominant in argillic to pyropylitic zones (Fig. 2C).

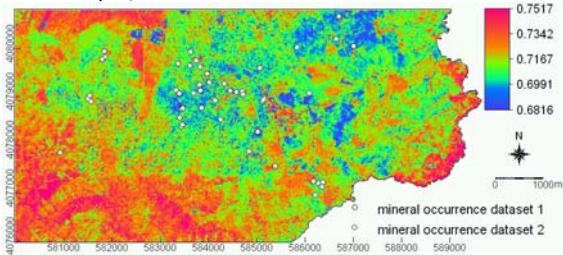
A. Band Ratio 1: arctan transformation on bands 103/107 ($2.100/2.171\ \mu\text{m}$).



B. Band Ratio 2: arctan transformation on bands 107/109 ($2.171/2.205\ \mu\text{m}$).



C. Band Ratio 3: arctan transformation on bands 118/112 ($2.357/2.258\ \mu\text{m}$).



D. Distance to fault and fracture. Increasing pixel brightness in this image indicates increasing distance from a fault or fracture.

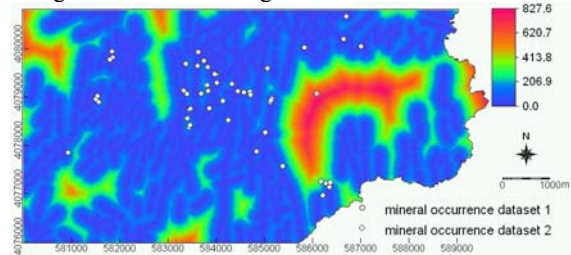


Figure 2: Input layers for WofE modeling. Map coordinates are in meters (UTM projection, zone 30N).

2.3 Data for Structural Evidence

Mapped faults and fractures were screen-digitized on georeferenced raster-scanned maps, which were obtained from published (IGME, 1981; Arribas et al., 1995) and unpublished sources. In addition, faults and fractures were interpreted and screen-digitized on shaded-relief images of a digital elevation model (DEM) derived from Advanced Spaceborne and Thermal Emission Radiometer (ASTER) data acquired on 26 May 2002. A map of distances to mapped and interpreted faults and fractures was then created (Fig. 2D) and used in WofE modeling.

2.4 Mineral Occurrence Data for WofE Modeling

Two sets of locations of mineral deposit occurrences were used in WofE modeling. One set, of 14 epithermal deposit occurrences, was digitized from a 1:50,000 scale geological map of Spain (IGME, 1981); and from a map in Arribas et al. (1995). The other set, of 47 epithermal deposit occurrences, was digitized from the mineral prospectivity map of Rigol-Sanchez et al. (2003), which actually shows 49 epithermal occurrences although two of these fall outside our study area. In this latter set, 11 epithermal deposit occurrences were discarded because each of them lie within 25 m of an epithermal deposit occurrence in the first set, which indicates high likelihood that these are the same 11 of the 14 in the first set. Each of the two sets of epithermal deposit occurrences were then used for training and for cross-validation of a WofE model. A training set is assumed to represent discovered mineral deposits, whereas a cross-validation set is assumed to represent undiscovered mineral deposits.

3. Methodology

3.1 Generation of Prospectivity Map: Weights-of-Evidence (WofE) Modeling

Initially, we created a mineral prospectivity map via the WofE method (Good, 1950), which is based on a Bayesian probability framework to update prior probability of occurrence of mineral deposits of the type sought in every unit cell or pixel in a study area. We used a set of training mineral deposit occurrences of the type sought (say D) and a number of thematic geological evidences (say B'_i with a threshold at t) having positive spatial association with such type of mineral deposits. The estimated prior probability of mineral occurrence is $P(D)$.

It can be shown that the weight of evidence for the presence of B' is $W^+ = \ln\left[\frac{P(B' | D)}{P(B' | \bar{D})}\right]$ and the weight of evidence for the absence of B' is $W^- = \ln\left[\frac{P(\bar{B}' | D)}{P(\bar{B}' | \bar{D})}\right]$ and the variances are given as

$$s^2(W^+) = \frac{1}{N(B' \cap D)} + \frac{1}{N(B' \cap \bar{D})} \quad \text{and} \quad s^2(W^-) = \frac{1}{N(\bar{B}' \cap D)} + \frac{1}{N(\bar{B}' \cap \bar{D})}$$

[1]

If $s^2(W_i)$ is either $s^2(W_i^+)$ or $s^2(W_i^-)$ then the variance of the posterior odds is defined as

$$s^2(O) = \sum_{i=1}^k s^2(W_i)$$

[2]

The output mineral prospectivity map is a map of posterior probability ($P_j = P_j(D | B_1, \dots, B_k)$) of occurrence of mineral deposits of the type sought. In such a map, we considered individual pixels to be prospective if their posterior probability is greater than the estimated prior probability. The posterior probabilities and prediction rate of WofE were used to determine the optimal exploration target zones.

3.2 Derivation of Focal Points and Target Zones

In order to derive optimal exploration target zones, the posterior probabilities in a mineral prospectivity map are used (a) to estimate a reasonable number of exploration focal points (or pixels) and (b) as weights in an objective function to derive optimal exploration focal points via simulated annealing (SA). Each of the optimal exploration focal points is then buffered with a reasonable distance in order to derive a set of optimal exploration target zones.

For (a) above, to estimate the number of exploration focal points, we employed the binomial distribution because mineral deposit occurrence is a binary variable, being either present or absent. Thus, estimation of n exploration focal points so as to discover at least r mineral deposit occurrences, with a probability of success p , at a 95% confidence, requires a solution for the following equation:

$$\sum_{i=r}^n \binom{n}{i} p^i (1-p)^{n-i} = 0.95$$

[3]

Deriving the optimal exploration focal points requires definition of an objective function, called the fitness function. For (b) above, for a two-dimensional region A divided into $N(A)$ unit cells, let the spatial configurations of n optimal exploration focal points be denoted by S^n . We denote the posterior probability of mineral deposit occurrence per unit cell in A derived from WofE modeling by $P(\vec{x}) = \{P_j(\vec{x}) | \vec{x} \in A\}$, where \vec{x} is the location vector of the unit cell in A , with a corresponding pixel in an image I , for unique condition j . In SA (Kirkpatrick et al., 1983), a fitness function $\phi(S^n): S^n \rightarrow \mathfrak{R}^+$, which is an extension to the Weighted Means Shortest Distance (WMSD)-criterion (Debba et al., 2005), is minimized to optimize the search for n exploration focal points.

$$\phi_{\text{WMSD+v}}(S^n) = \frac{\lambda}{N(A)} \sum_{\vec{x} \in A} \binom{n}{i} P(\vec{x}) \|\vec{x} - Q_{S^n}(\vec{x})\| + (1-\lambda) s^2(O_{S^n})$$

where $Q_{S^n}(\vec{x})$ is the location vector of an optimal exploration focal point in S^n nearest to \vec{x} , and $s^2(O_{S^n})$ is the variance of the posterior odds at every optimal exploration focal point in S^n . The objective function optimized, considered not only the magnitude of the posterior probability but also the uncertainty of the posterior probability. The $\lambda \in [0,1]$ is a constant controlling the effect of the posterior probability and the variance of the posterior odds in finding and selecting optimal exploration focal points.

4. Results and discussion

The study area consists of 65253 unit cells of 25×25 m, based on the spatial resolution of the ASTER DEM. All the maps/images used in the analyses were resampled to this spatial resolution, which is adequately small and appropriate for WofE modeling (Agterberg, 1992). The estimate of $P(D)$ based on training set 2 is 0.00055. Based on prospective pixels and on training set 2, the WofE model derived has a prediction rate of 0.64. The rather low prediction rate (of 64%) of the probabilistic prospectivity map shown in Figure 3 is attributable partly to the (a) small number of evidential datasets used and (b) presence of two (precious- and base-metal) sub-types of epithermal deposits used in modeling prospectivity.

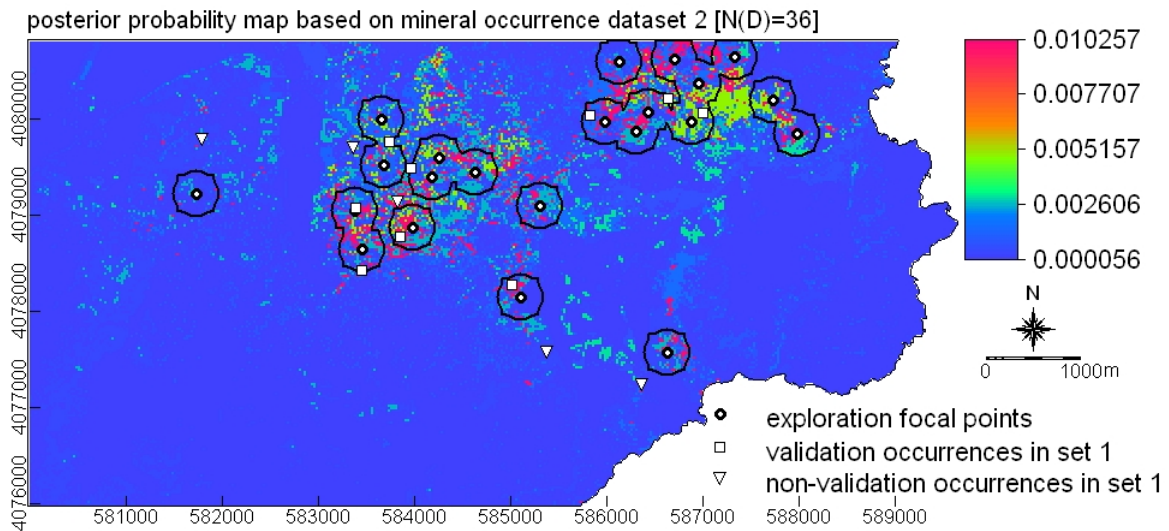


Figure 3: Optimal exploration target zones defined by buffering to 238m each of the optimal

We estimated the number of exploration focal points by solving for n in Equation 3. We first assumed that $r = 9$ based on the nine predicted out of 14 undiscovered epithermal occurrences in training set 1 and that $p = 0.0025$ based on the average posterior probabilities of prospective pixels in the input WofE prospectivity model. With these assumptions we derive $n = 6280$. This number of exploration focal points is intractable. However, we interpret and show later that 6280 is approximately the total number of unit cells within plausible exploration target zones. Instead of $p = 0.0025$, we used $p = 0.6$ based on the approximate prediction rate of the input WofE model. Accordingly, $n = 22$, which is a plausible number of exploration focal points as centroids of individual exploration target zones wherein to search further for the nine (assumed) undiscovered epithermal deposit occurrences.

By using the posterior probability map as input and by specifying $n = 22$ and $\lambda = 0.5$ in Equation 4, the locations of the optimal exploration focal points were derived. The value of $\lambda = 0.5$ was chosen instead of being estimated automatically in order to avoid computational time. Each of the derived optimal exploration focal points (Fig. 3) occupies a unit cell with the highest posterior probability value based on training set 2 in a circular neighborhood of unit cells with posterior probabilities greater than the prior probability estimate. Each of the derived optimal exploration focal points does not fall exactly on but is proximal to a unit cell representing an undiscovered

epithermal mineral deposit occurrence belonging to the set of epithermal deposit occurrence data in training set 1.

In order to define optimal exploration target zones around each of the derived optimal exploration focal points, the following analysis was performed. We quantified proximity to an undiscovered deposit occurrence by utilizing the estimated number of 6280 unit cells required to delineate the nine predicted out of the 14 cross-validation deposit occurrences and using $p = 0.0025$ in Equation 3. The total area represented by the 6280 unit cells is approximately $6280 \times 252 = 3925000 \text{ m}^2$. If each of the nine undiscovered deposit occurrences, predicted by the WofE model, out of the 14 cross-validation undiscovered deposit occurrences, is within a delineated sub-area of $3925000/22 = 178409 \text{ m}^2$ containing each of the optimal exploration focal points, then this indicates that an optimal exploration target zone is proximal to at least one undiscovered deposit occurrence. This also means that, if each of the nine predicted undiscovered deposit occurrences, delineated by the WofE model, out of the 14 cross-validation undiscovered deposit occurrences, is within a radius of $\sqrt{178409/\pi} = 238 \text{ m}$ (area of circle = $\pi \times \text{radius}^2$) around a derived optimal exploration focal point, then an optimal exploration focal point is in close proximity to at least one undiscovered deposit occurrence.

Each of the 22 derived optimal exploration focal points was then buffered with a radius of 238 m in order to delineate optimal exploration target zones. Seven of the nine (assumed) undiscovered deposit occurrences, delineated by the WofE model out of the 14 cross-validation undiscovered deposit occurrences, are within the delineated optimal exploration target zones. The result of this analysis indicates that the derived optimal exploration focal points are proximal to undiscovered epithermal deposit occurrences. The average of posterior probabilities of unit cells within each of the delineated optimal exploration target zones is 0.010, which is higher than the average posterior probability (0.0024) of unit cells representing discovered epithermal deposit occurrences (training set 2) and the average posterior probability (0.0029) of unit cells representing (assumed) undiscovered epithermal deposit occurrences (training set 1).

These indicate that the algorithm is efficient in finding and selecting optimal exploration focal points in prospective ground. The results also suggest that within the delineated exploration target zones there is much higher probability of mineral deposit occurrence than would be expected due to chance, which is translatable theoretically to increased chance of mineral deposit discovery.

Until now, there is no objective procedure for demarcating and prioritizing of new exploration target zones based on regional- to district-scale mineral prospectivity maps that have been determined subjectively. That is, portions of predicted prospective ground that are distal to and not containing discovered mineral deposit occurrences are considered, based on subjective judgement, new exploration target zones. In this study, new exploration target zones are determined based on the spatial distribution of estimated posterior probabilities of mineral deposit occurrence, which are used as weights in an objective function in SA to determine optimal exploration focal points.

In district-scale mineral prospectivity mapping, as in the present case study, one does not aim to define drilling targets as individual pixels but prospective zones defined by neighborhood of pixels of high prospectivity for further exploration work. Therefore, after deriving optimal exploration

focal points as individual pixels based on a probabilistic mineral prospectivity map, we defined exploration target zones around them. The analysis presented is based upon available datasets and geo-information derived from them, but avoids subjective expert opinion.

5. Conclusions

The proposed methodology provides for objectively, and with reasonable accuracy, demarcation and selection of optimal exploration target zones for further investigation of undiscovered mineral deposit occurrences based on a given probabilistic mineral prospectivity map. In the study area, nine out of 14 (assumed) undiscovered epithermal deposit occurrences, predicted correctly by a WofE predictive model of mineral prospectivity, are either within or at most 30 m away from a buffered zone of an optimal exploration focal point.

References

- Agterberg, FP 1992, 'Combining indicator patterns in weights of evidence modeling for resource evaluation', *Nonrenewable Resources*, vol. 1, no. 1, pp 39–50.
- Arribas, A Jr., Cunningham, CG, Rytuba, JJ, Rye, RO, Kelley, WC, Podwysoki, MH, McKee, EH & Tosdal, RM 1995, 'Geology, geochronology, fluid inclusions, and isotope geochemistry of the Rodalquilar gold alunite deposit, Spain', *Economic Geology*, vol. 90, pp. 795–822.
- Cudahy, T, Okada, K & Brauhart, C 2000, 'Targeting VMS-style Zn mineralisation at Panorama, Australia, using airborne hyperspectral VNIR-SWIR HyMap data', in *ERIM Proceedings of the 14th International Conference on Applied Geologic Remote Sensing*, Las Vegas, pp. 395–402.
- Debba, P, van Ruitenbeek, F, van der Meer, F, Carranza, EJM & Stein, A 2005, 'Optimal field sampling for targeting minerals using hyperspectral data', *Remote Sensing of Environment*, vol. 99, no. 4, pp 373–386.
- Good, IJ, 1950, *Probability and the Weighing of Evidence*, Griffin, London.
- IGME 1981, *Mapa Geologico de Espaa, Carboneras, 1.046/24-43; El Pozo de los Frailes, 1.060/24-44, e. 1:50,000. Instituto Geologico y Minero de Espaa, IGME, Servicio de Publicaciones, Ministerio de Industria y Energia, Madrid.*
- Kirkpatrick, S, Gelatt, CD Jr. & Vecchi, MP 1983, 'Optimization by Simulated Annealing', *Science*, vol. 220, no. 4598, pp. 671–680.
- Kruse, FA 2002, 'Comparison of AVIRIS and Hyperion for hyperspectral mineral mapping', in *SPIE Aerospace Conference*, 9-16 March 2002, Big Sky, Montana, published on CD-ROM, IEEE Catalog Number 02TH8593C, Paper 6.0102, pp. 1–12.
- Lillesand, TM, Kiefer, RW & Chipman, JW 1994, *Remote Sensing and Image Interpretation*, New York, John Wiley & Sons.
- Rigol-Sanchez, JP, Chica-Olmo, M & Abarca-Hernandez, F 2003, 'Artificial neural networks as a tool for mineral potential mapping with GIS', *International Journal of Remote Sensing*, vol. 24, no. 5, pp. 1151–1156.